NeuroImage 164 (2018) 100–111

Contents lists available at ScienceDirect

NeuroImage

journal homepage: www.elsevier.com/locate/neuroimage

Laminar imaging of positive and negative BOLD in human visual cortex at 7 T

Alessio Fracasso[a,b,*], Peter R. Luijten[a], Serge O. Dumoulin[b,c,1], Natalia Petridou[a]

[a] Radiology, Imaging Division, University Medical Center Utrecht, Utrecht, Netherlands
[b] Spinoza Centre for Neuroimaging, Amsterdam, Netherlands
[c] Experimental Psychology, Helmholtz Institute, Utrecht University, Utrecht, Netherlands

ABSTRACT

Deciphering the direction of information flow is critical to understand the brain. Data from non-human primate histology shows that connections between lower to higher areas (e.g. retina→V1), and between higher to lower areas (e.g. V1←V2) can be dissociated based upon the distribution of afferent synapses at the laminar level. Ultra-high field scanners opened up the possibility to image brain structure and function at an unprecedented level of detail. Taking advantage of the increased spatial resolution available, it could theoretically be possible to disentangle activity from different cortical depths from human cerebral cortex, separately studying different compartments across depth.

Here we use half-millimeter human functional and structural magnetic resonance imaging (fMRI, MRI) to derive laminar profiles in early visual cortex using a paradigm known to elicit two separate responses originating from an excitatory and a suppressive source, avoiding any contamination due to blood-stealing. We report the shape of laminar blood level oxygenation level dependent (BOLD) profiles from the excitatory and suppressive conditions. We analyse positive and negative %BOLD laminar profiles with respect to the dominating linear trend towards the pial surface, a confounding feature of gradient echo BOLD fMRI, and examine the correspondence with the anatomical landmark of input-related signals in primary visual cortex, the stria of Gennari.

Introduction

Human cortex is organized in layers that differ in morphology, connectivity and function (Callaway, 1998; Lund, 1988; Zilles et al., 2004). This laminar organization was initially observed in primary visual cortex (V1), where heavily myelinated retino-cortical afferents terminate predominantly in granular layers giving rise to the stria of Gennari (1782). In principle, a laminar profile of the first synaptic activity would reveal the location of input activity in primary visual cortex (V1). Non-human primate studies have shown that the laminar distribution of afferent synapses in early visual areas dissociate connections between lower to higher areas (feed-forward activity, e.g. retina→V1, terminating in granular layers), and between higher to lower areas (feed-back activity, e.g. V1←V2, terminating in supra-granular and infra-granular layers, (Angelucci et al., 2002; Felleman and Van Essen, 1991). Until recently investigations on functional laminar cortical organization were restricted to (invasive) animal research. The advent of ultra-high field human MRI scanners (7 T and beyond) has opened up the possibility to study and visualize finer scales of organization of the human cortex, thanks to the increased imaging resolution achievable without considerable loss in signal-to-noise ratio, bridging the gap between (invasive) animal research and human imaging.

Laminar synaptic activity might reflect suppressive or excitatory processes, and the relationship between the blood oxygenation level dependent (BOLD) signal and these processes is not straightforward. It has been shown, however, that the positive BOLD signal is related to synaptic activity at a given location, as shown by the correlation between BOLD amplitude and local field potentials (Logothetis et al., 2001). In addition, a close correlation has been reported between the negative BOLD signal and localized decreases in neural spiking, suggesting that neuronal suppression might be a major driving source of the negative BOLD response (Shmuel et al., 2006). In principle, BOLD signals across cortical depth could reflect suppressive or excitatory processes given sufficient sensitivity and specificity to the micro-vasculature that directly interfaces with neural tissue.

* Corresponding author at: Radiology, Imaging Division, University Medical Center Utrecht, Utrecht, Netherlands.
E-mail address: A.Fracasso-2@umcutrecht.nl (A. Fracasso).
[1] Co-senior author.

http://dx.doi.org/10.1016/j.neuroimage.2017.02.038
Accepted 13 February 2017
Available online 14 February 2017

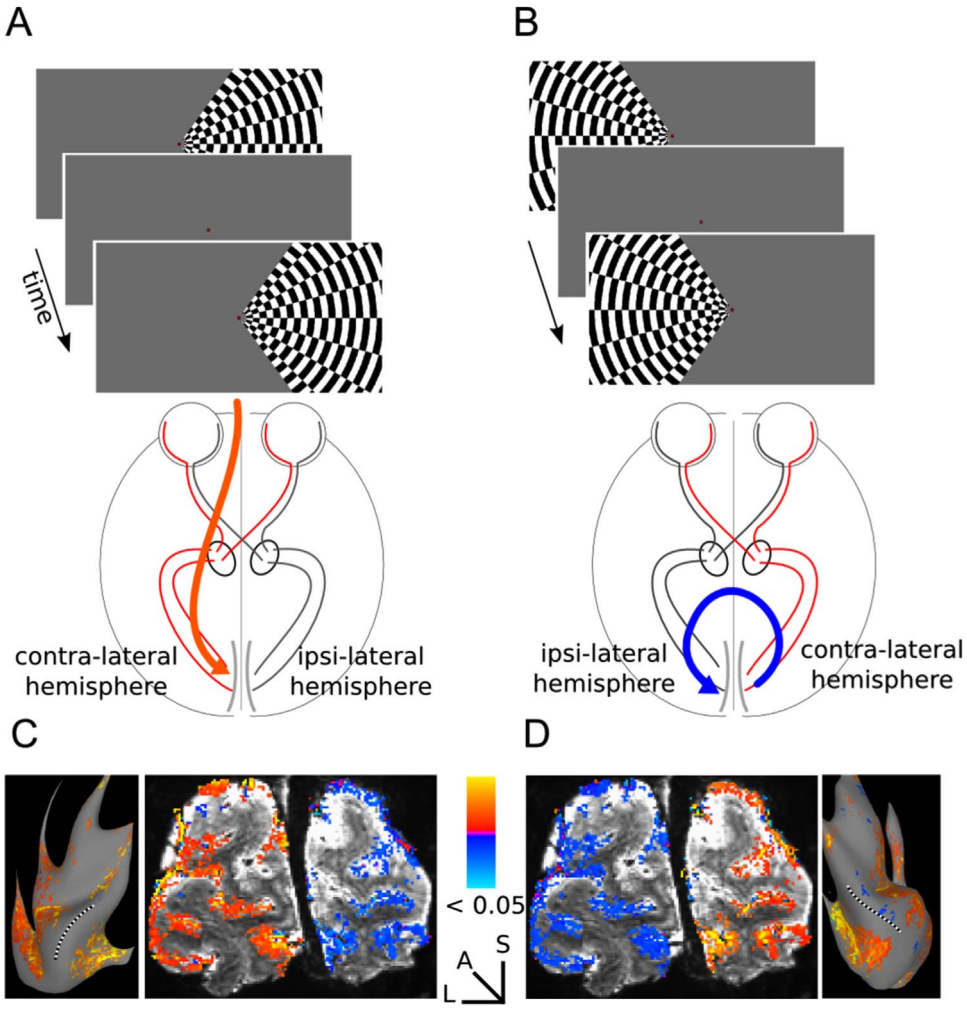

Fig. 1. Visual stimulation and signal sources. On different runs, different visual hemifields were stimulated by a contrast-defined lateralized dart-board pattern (panels A and B). The alternate segments of the pattern moved in opposite radial directions and the motion direction changed unpredictably. Participants reported motion-direction changes while maintaining central fixation. β coefficient maps elicited by viewing the stimulus shown in panels A and B are shown in panels C and D, respectively, for one representative participant. These activation maps consist of signal amplitude (expressed as β coefficient from the generalized linear model, GLM) thresholded by cluster size and mean Student's T statistic (cluster > 20, threshold by $T > 2$, $p < 0.05$, uncorrected). For the ipsi-lateral condition (in blue) β coefficients are not thresholded based on the corresponding T statistic, but are reported for the voxels selected based on the contra-lateral (positive %BOLD) visual stimuli condition. Changing the stimulus hemifield allows us to record contra-lateral (positive %BOLD) and ipsi-lateral (negative %BOLD) from the same voxels in different runs. The insets on panels C and D represent the 3D-mesh from the left and right hemisphere of the visual cortex, respectively, for the same participant, built from the level-set volume representing the middle of cortical depth, inflated for visualization purposes. β coefficient maps over the surface are reported for those nodes on the surface where the mean T-value for the contra-lateral condition along each separate BOLD profile across cortical depth exceeded 2 ($p < 0.05$, uncorrected, see Laminar Profiles, selection). Dashed black and white lines represent the dorsal V1/V2 border based on visual field mapping results (see section 'Visual field mapping'), the ventral V1/V2 border is not visible from the same view. Please note the under-representation of the vertical meridian on the reconstructed occipital surfaces, as could be expected given by the lack of visual stimulation along the vertical meridian in the visual stimuli adopted during the experiment, see panels A and B.

Several recent human studies investigated the laminar variation of the functional MRI (fMRI) signal, using spatial resolutions spanning from ~0.75 to ~1.5 mm with gradient-echo (GRE) and spin-echo (SE) BOLD, providing insights on the specificity and sensitivity of the BOLD signal between different vascular compartments across cortical depth (Chen et al., 2012; De Martino et al., 2013; Fracasso et al., 2016a; Koopmans et al., 2011, 2010; Olman et al., 2012; Polimeni et al., 2010; Ress et al., 2007; Siero et al., 2013, 2011). Promising attempts have been also made using vascular space occupancy (VASO) and calibrated BOLD sequences, across different species, showing improved specificity to the capillary bed across cortical depth (Guidi et al., 2016; Huber et al., 2015, 2014; Jin and Kim, 2008). In the context of MRI and fMRI we use the term 'laminar' to indicate a measure taken along cortical depth, from the gray matter/white matter border to the gray matter/cerebrospinal fluid border, as opposed to measurements from the 6 cyto-architectonically defined layers of human neocortex.

FMRI at the sub-millimeter scale poses a number of challenges from the data-acquisition and data-analysis perspectives. The human brain is more gyrified than animal brains, and the use of isotropic resolutions is highly desirable. Cortical thickness is not uniform across the cortex and is biased, being thicker in sulci as compared to gyri (Waehnert et al., 2016, 2014). The convoluted folding of the human cortex gives rise to another potential issue for sub-millimeter functional imaging: it has been shown that %BOLD signal changes vary as a function of the angle between the cortical surface and B0 (Gagnon et al., 2015), due to the presence of large pial veins oriented parallel to the cortical surface.

In this investigation we push the functional resolution further to 0.55 mm isotropic using a 3D gradient echo, echo planar imaging sequence (3D-EPI) and custom-built high density surface coil receive arrays (Petridou et al., 2013), to examine the positive and negative BOLD signal across cortical depth. We used a visual stimulation paradigm consisting of a unilateral section of a dart-board pattern, which is known to elicit spatially separated responses from 2 sources (Tootell et al., 1998): BOLD signal increase on the contra-lateral visual cortex (positive %BOLD with respect to visual stimulation) and BOLD

signal decrease on the ipsilateral visual cortex (negative %BOLD, with respect to visual stimulation). This paradigm allows us to record responses dominated by positive and negative BOLD response amplitudes from the same portion of visual cortex in consecutive fMRI runs. fMRI data were accompanied by 0.5 mm isotropic resolution T1-weighted data acquired using a magnetization prepared rapid acquisition gradient recalled echo (MPRAGE) sequence (Bock et al., 2009; Fracasso et al., 2016b, 2016c) optimized for high contrast in myelin content within human cortex. We employed the equi-volume model approach to build a coordinate system along cortical depth taking local curvature into account, and investigated the shape of laminar BOLD profiles for the positive and negative BOLD signal conditions. We analyse positive and negative %BOLD laminar profiles with respect to the dominating linear trend towards the pial surface due to the presence of pial veins (a confounding feature of GRE BOLD), examine the correspondence of deviations from the linear trend with the location of the stria of Gennari, and assess the relationship between BOLD amplitude and the angle between the cortical surface and B0 (Gagnon et al., 2015), along cortical depth.

Materials and methods

Participants

Five males participated in the experiment, one participant was scanned twice, three participants were naïve to the experiment purpose (age range 25–39 years). One participant was left handed. All participants have normal or corrected-to-normal visual acuity. All participants were experienced with the MRI environment. All experimental procedures were conducted in accordance with the 1964 Declaration of Helsinki (most recently amended in 2008, Seoul), and cleared by the ethics committee of University Medical Center Utrecht.

Visual stimuli setup

Visual stimuli were presented by back-projection onto a 15.0×7.9 cm screen inside the MRI bore. Participants viewed the display through prisms and mirrors, and the total distance from the participant's eyes (in the scanner) to the display screen was 35 cm. Display resolution was 1024×538 pixels.

Stimuli

The stimuli were generated in Matlab (Mathworks, Natick, MA, USA) using the PsychToolbox (Brainard, 1997; Pelli, 1997). Participants fixated in the center of the screen. The contrast-defined stimulus consisted of a unilateral dart-board pattern avoiding a central circular region (0.4° of visual angle) and displaced by 20° of polar angle from the vertical meridian (Fig. 1A, B). The stimulus radius was 3.5° of visual angle. The dart-board consisted of a rectangular grid with a spatial frequency of 0.5° of visual angle. Spokes of the dart-board pattern moved in opposite radial directions. The motion-direction of the spokes changed unpredictably with an inter-stimulus interval (ISI) of 600 ms ± 200 ms (frequency of change ~1.7 Hz). All spokes changed direction simultaneously. Participants reported motion-direction changes while maintaining central fixation (percent correct: mean=70%, standard deviation=6%, n=6). Unilateral stimuli were presented on a gray background for 13 s, followed by full field mean luminance for 26 s, to allow the hemodynamic response to return to baseline before the subsequent visual stimulation. The stimulus side changed on every run. For each run, 7 cycle repetitions were presented.

Visual field mapping

The primary visual cortex was reconstructed using near-identical procedures as in previous studies (Amano et al., 2009; Dumoulin and Wandell, 2008; Harvey and Dumoulin, 2011; Winawer et al., 2010). Stimuli consisted of drifting bar apertures at four orientations, which exposed a checkerboard pattern moving parallel to the bar orientation (Dumoulin and Wandell, 2008). Alternating rows of checks moved in opposite directions, and orthogonally with respect to the bar orientation. The bar width (and width of alternating white and black checks) subtended one-quarter of the stimulus radius (1.56° of visual angle). The bar moved across the stimulus aperture in 20 evenly spaced steps, each 0.625° of visual angle, 1/20th of the stimulus window diameter. As there was one step at the start of each functional volume acquisition, each pass of the stimulus lasted 20 acquisition repetitions (TRs), 30 s. Four bar orientations and two different motion directions for each bar were presented, giving a total of eight bar motion directions (upward, downward, left, right, and four diagonals) within each run (the same stimuli order was presented for each run). After each horizontal or vertical bar orientation pass, a 30 s of mean-luminance (zero contrast) stimulus was displayed. Four mean-luminance blocks were presented at regular intervals during the scan. Participants fixated on a dot in the center of the visual stimulus. The model estimates a population receptive field (pRF) for every voxel using a method previously described (Dumoulin and Wandell, 2008). We used the position estimates of the pRF to define V1. Area V1 was defined on T1-weighted anatomical MRI data with a voxel size of 0.8×0.8×0.8 mm (resampled at 1 mm isotropic). The T1-weighted volume was co-registered with the high resolution 0.5 mm isotropic T1-w images (see *High resolution MRI and fMRI acquisition* below) using the function 3dAllineate and a rigid transformation and the borders of V1 were ported to the high resolution 0.5 mm isotropic space using the associated transformation matrix. Repetition time (TR) was 7 ms, echo time (TE) was 2.84 ms and flip angle was 8°. Functional T2*-weighted multi-slice echo-planar images (EPI) were acquired using a Philips Achieva 7T scanner (Best, Netherlands), a volume transmit coil for excitation and a 32-channel head coil for signal reception (Nova Medical, MA, USA). Acquisition parameters were: TR/TE: 1500/30 ms, flip angle: 70°, voxel size: 2 mm isotropic, and 24 coronal slices with no gap, FOV: 50×190×190, EPI factor: 47, covering the occipital lobe. Functional scans were each 248 time frames (372 s) in duration, and the first eight time frames were discarded to ensure that signal had reached steady state.

High resolution MRI and fMRI acquisition

High resolution anatomical and functional data were acquired using a Philips Achieva 7 T scanner (Philips, Best, Netherlands) with a maximum gradient strength and slew rate of 40 mT/m and 200 T/m/s respectively, using a volume transmit coil for excitation (Nova Medical, MA, USA) for all scans described below.

Anatomical T1-weighted MRI images (T1-w) were obtained with the 32-channel receive head coil (Nova Medical, MA, USA) and a 3-dimensional MPRAGE sequence adjusted to obtain a strong myelin contrast in gray matter (Bock et al., 2009; Fracasso et al., 2016b, 2016c). A strong contrast in high myelin content gray matter was obtained by setting the time delay (TD) between inversion pulses such that the difference in longitudinal magnetization prior to the inversion pulse was increased between white and gray matter, and by setting the inversion delay (TI) such that the gray matter signal was just above the null point. An optimum contrast is obtained at TD=6 s and TI=1200 ms. Other sequence parameters were: TR/TE: 8/3 ms, flip angle: 8°, voxel size=0.5 mm isotropic, 60 coronal slices, FOV: 140×140×30 mm, bandwidth 202 Hz/px, turbo factor: 275, adiabatic inversion, and scan duration ~7.5 min. The imaging volume was at about the same location in visual cortex as the functional images. 4–6 scans were acquired per participant and the session lasted about 1 h. These images served as the basis for the cortical surface extraction and stria of Gennari identification. A proton density scan was also acquired on the same FOV as the T1-w data with the following parameters: 3D turbo-field echo, TR/TE: 9/2 ms, FOV: 140×140×30 mm, flip an-

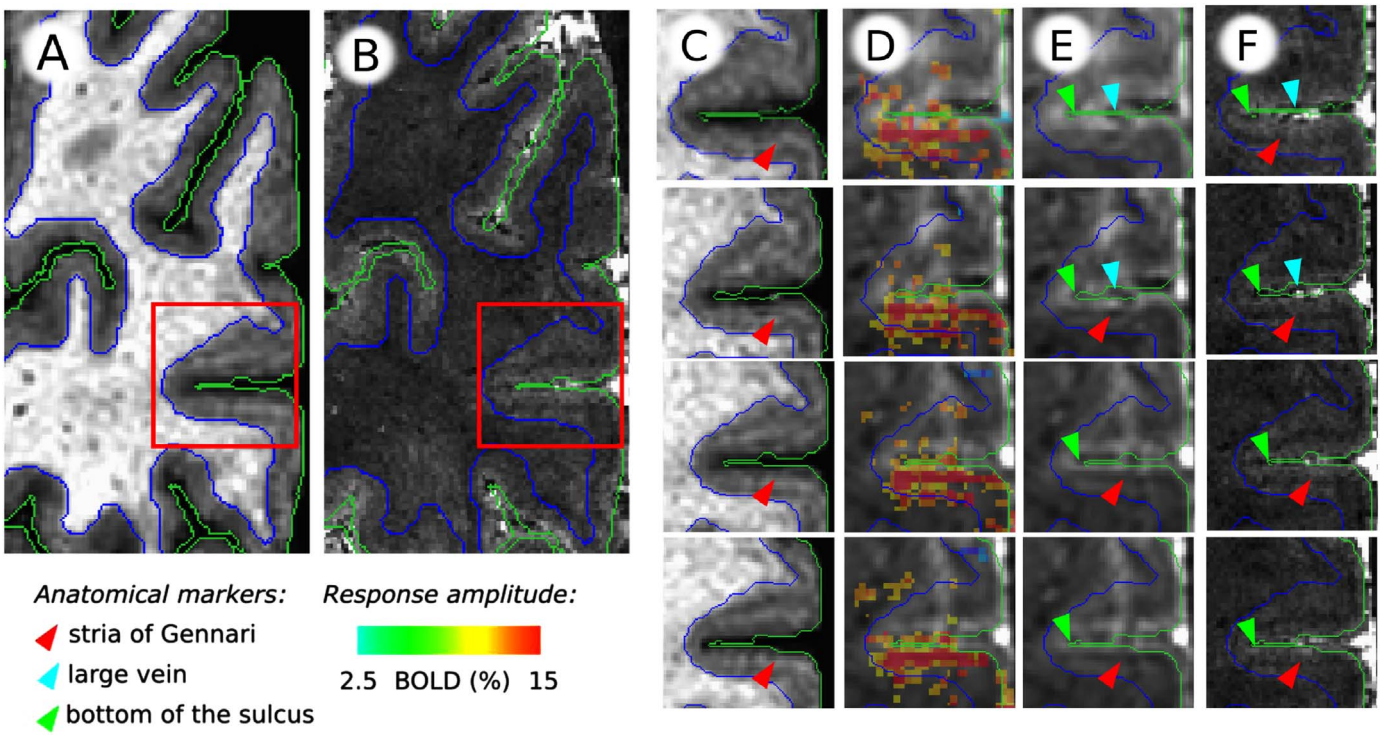

Fig. 2. Anatomical and functional images. A, B) T1-weighted and T2*-weighted images (left hemisphere) are shown for a coronal slice. Red square represents the location around the calcarine sulcus enlarged in panels C–F. The blue and green lines represent the GM/WM and GM/CSF border respectively. C shows the T1-weighted image, D shows the mean 3D-EPI image obtained from the functional time series ('functional' 3D-EPI) with the superimposed β coefficient map, elicited by the contra-lateral condition (positive %BOLD, cluster size > 20, thresholded by $T > 2$, $p < 0.05$, uncorrected, color scale shown at the bottom left of the figure: 'Response Amplitude'). E shows the mean functional 3D-EPI image, without the superimposed β coefficient map. F shows the T2*-weighted-w anatomy. Arrows with different color point to different anatomical features, in corresponding locations between the images. The stria of Gennari (red arrows, see legend on the bottom left of the figure, 'Anatomical markers') appear dark in T2*- weighted and mean 'functional' 3D-EPI images, whereas it appears bright in T1-weighted images. The large veins (cyan arrows) appear dark in the T2*-w weighted and mean 3D-EPI images. The bottom of the sulci (green arrow), is also indicated. For visualization, data shown is upsampled to the highest acquisition resolution (0.3 mm isotropic for the T2*-w weighted anatomy), in this way the same slice is shown for the different contrasts.

gle=1°, voxel size: 1×1×1 mm^3, 30 coronal slices, BW: 506 Hz/px, no acceleration.

On the second session, functional T2*-weighted 3-dimensional segmented echo planar images (3D-EPI) were acquired using two custom-built high-density 16-channel surface coils (total 32 channels) for signal reception (Petridou et al., 2013). The sequence parameters were: TR/TE=54/27 ms, acceleration factor using SENSE encoding: 3.5 (right-left)×1.5 (anterior-posterior), echo planar factor: 19, readout duration ~53 ms, 3 segments, 120 shots per volume, bandwidth in the phase encoding direction: 21 Hz/px (potential blurring, i.e., loss of spatial resolution, in the right-left phase-encode direction estimated at ~15% with an assumed T2* in gray matter of 28 ms, Haacke et al., 1999), flip angle: 20°, resolution=0.55 mm isotropic, 40 coronal slices, FOV=120×130 mm^2. Functional volumes were acquired every 6.5 s and functional scans were each 46 time frames (299 s) in duration, of which the first 2 time frames (13 s) were discarded to ensure the signal was at steady state. 6 to 8 runs were acquired for each participant with half runs using left and half runs using right unilateral stimuli. Left visual stimuli and right visual stimuli runs were interleaved. Participant 1 participated in two functional sessions.

A very high resolution T2* anatomical scan was acquired for one participant (P1) using the 16-channel surface coils and 3D-EPI with the following parameters: TR/TE: 82/30 ms, resolution: 0.3 mm isotropic, 133 coronal slices, FOV 40×171×170 mm, EPI factor 11, SENSE=3 right-left, scan duration 197 s/run, flip angle: 19°. 5 runs were acquired.

Preprocessing of high resolution anatomical and functional images

T1-w images were corrected for head movement between scans using the AFNI (http://afni.nimh.nih.gov, Cox, 1996) 3dAllineate function, using 6 degrees of freedom and imposing wsinc5 as the final interpolation step. Motion corrected volumes were averaged together to increase SNR. Proton density volumes were re-sampled to the T1-w volume space. The average T1-w image was divided by the proton density volume to correct for B1 field inhomogeneities. Segmentation of the T1-w images was performed manually using ITKGray (https://web.stanford.edu/group/vista/cgi-bin/wiki/index.php/ItkGray).

fMRI preprocessing was performed in AFNI. For computation of the head movement between scans, the first functional volumes for each scan were aligned using the function 3dvolreg. Within-scan motion correction was computed by aligning all the frames of a run to the first frame. Between and within scan motion correction was applied in a single step. The 3D-EPI mean image was obtained by averaging together all the motion corrected volumes in a session. The 3D-EPI mean image was registered to the motion-corrected and averaged T1-w images using an affine transformation via the function 3dAllineate. The coregistration was divided in three separate steps. In the first step the T1-w anatomy was clipped in the anterior-posterior direction, leaving only the occipital lobe. To provide a good starting point for the following coregistration, the mean 3D-EPI image was centered on the clipped anatomy using their respective centers of mass. Second, the mean 3D-EPI image was registered to the motion-corrected and averaged T1-w images using an affine transformation via the function 3dAllineate, first allowing for a large rotation – shift, and then refining the alignment using an affine transformation (using the two pass option in AFNI 3dAllineate). In the third step, the resulting coregistered mean 3D-EPI image was further optimized allowing only a small amount of movement, using an affine transfor-

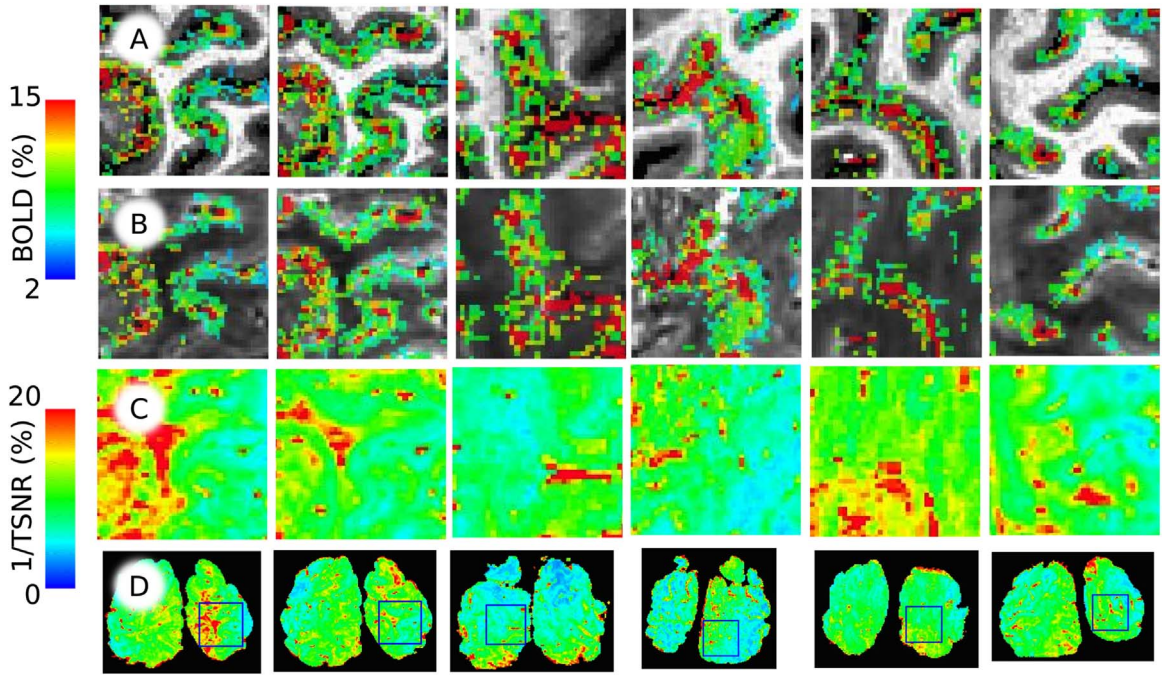

Fig. 3. General linear model maps overlaid on the T1-weighted and mean 3D-EPI images. Row A, shows a portion of the calcarine sulcus on the T1-w images for all the participants (across columns) with the response amplitude superimposed (β coefficient map, elicited by the contra-lateral condition, positive %BOLD, cluster size > 20, thresholded by $T > 2$, $p < 0.05$, uncorrected, color scale shown at the left of the figure). Row B, location and overlay as in row A, but with mean 3D-EPI as underlay. Row C shows the 1/TSNR (%) map from the same location as rows A and B. Row D shows the 1/TSNR (%) map from the complete slice for each participant, the blue box indicates the calcarine location reported in rows A, B, C; a low value corresponds to improved signal stability and fMRI detectability.

mation. The obtained transformations were combined in a single affine matrix by matrix multiplication.

By default, the coregistration procedure started using local Pearson correlation as the cost function. In case it did not give a satisfactory result, evaluated by visual inspection, alternative cost functions were adopted (mutual information and normalized mutual information). In most cases local Pearson correlation gave the best results (Saad et al., 2009). Our main priority was to obtain an optimal co-registration results around the calcarine sulcus. Co-registration output was visually checked by evaluating the location of anatomical markers as gray matter/white matter (GM/WM) and gray matter/cerebro-spinal fluid (GM/CSF) boundaries in the calcarine sulcus and by the correspondence of the position of large vessels between the T1-w and the mean 3D-EPI image.

The same coregistration strategy was adopted for the T2*-w anatomical images acquired for participant P1; the volume was interpolated on the T1-w image space using nearest-neighbor interpolation and a 0.3 mm isotropic grid, to preserve the anatomical details in the image as much as possible.

In Figs. 2 and 3 we report images of the coregistered volumes, overlaid with BOLD amplitude maps (Figs. 2C, D; 3A, B).

Analysis of fMRI data

Functional MRI data were analyzed using a general linear model (GLM). Percentage signal change from baseline for each voxel on the positive %BOLD and negative %BOLD conditions was estimated using AFNI's 3dDeconvolve function. Nuisance regressors were modeled using polynomials up to the second order to remove any linear and quadratic trends, as well as the six motion parameters estimated during motion correction. All the participants taking part on the experiment were experienced with the MRI environment and motion in the scanner was minimal (average maximum translation from baseline image, first image in the session: 0.9 mm ± 0.42 mm). The GLM analysis was performed on the native 3D-EPI space. GLM maps obtained from the 3D-EPI space (T-maps and beta-coefficient-maps) and the 3D-EPI mean image were interpolated to the T1-w space using the affine matrix estimated in the registration step via nearest-neighbor interpolation (see *'Preprocessing of high resolution anatomical and functional images'*). In this way, we avoided interpolating the motion corrected time series to match the anatomical space, reducing the number of interpolation steps to two: motion correction step and interpolation on the T1-w volume (via nearest-neighbor interpolation).

We investigated the signal stability by computing the 1/TSNR. Given that we do not have a resting state block during which to estimate 1/TSNR, we report 1/TSNR measurements for all the participants of the study after estimating the GLM. TSNR is computed as average(signal)/stdev(noise). The "signal" is the 3D-EPI intensity, motion corrected, concatenated and scaled, the 'noise' are the GLM residuals after GLM fit. 1/TSNR values are reported as a percentage (multiplied by 100), with lower values indicating better signal stability (Petridou et al., 2013). In Fig. 3 we report 1/TSNR(%) maps and insets from the calcarine fissure. (1/TSNR %, Fig. 3 C, D).

Extraction of laminar profiles

The manual segmentation of the high resolution T1-w images was analyzed with CBS-tools (www.nitrc.org/projects/cbs-tools/, (Bazin et al., 2007)) in MIPAV (http://mipav.cit.nih.gov/). A volume-preserving distance map was computed between the GM/WM border and the GM/CSF border (Waehnert et al., 2014) in 16 separate level-set volumes. This approach provides a coordinate system of cortical depth which is independent of the cortical folding. For each of the 16 level-sets a 3D mesh was generated using the function IsoSurface in AFNI. Cortical thickness was estimated from CBS-tools. A region of interest (ROI) was selected based on the extent of each participant's V1, derived from pRF mapping (see *'Visual field mapping'*).

All the nodes on the surface corresponding to V1 were selected. For each node on the 3D mesh located at the middle of the cortical depth, a laminar profile was generated by iteratively growing the normal vector of the node to intersect the closest node on the 3D mesh towards the CSF and storing the corresponding node coordinates. The procedure

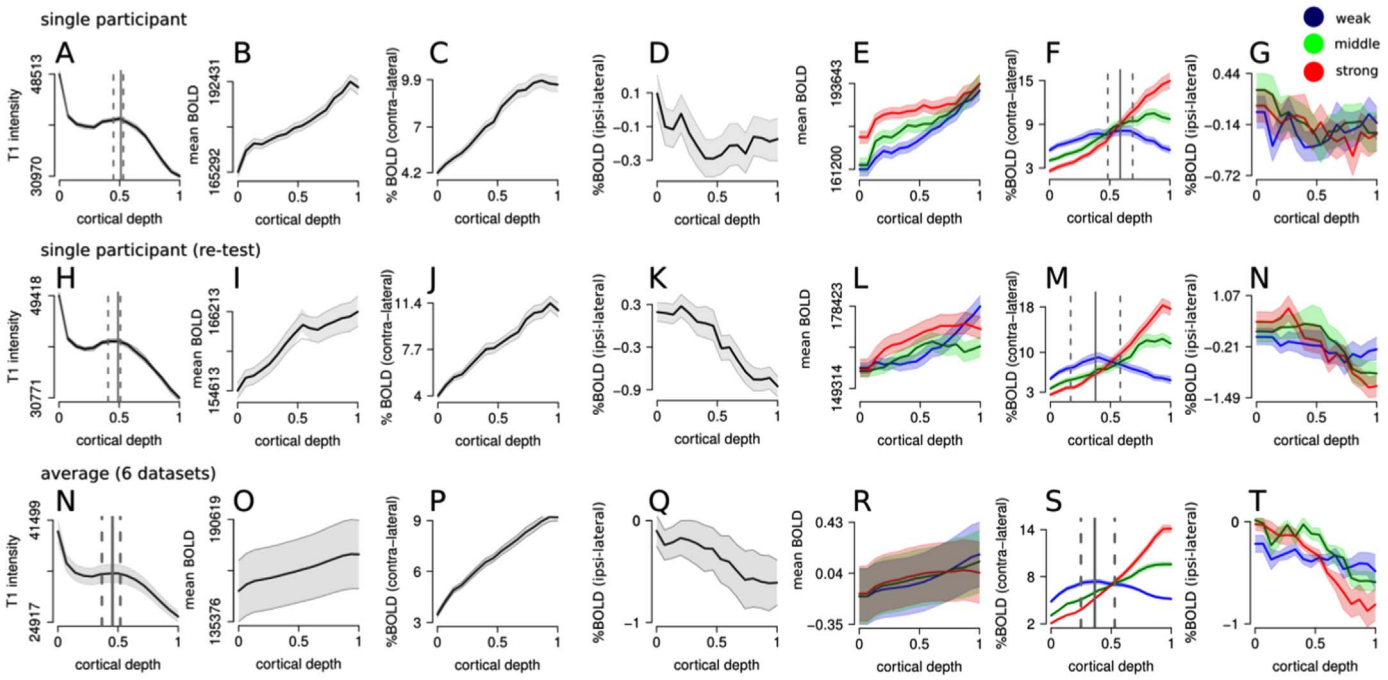

Fig. 4. Structural and functional intensity profiles across cortical depth. The x-axis ranges from 0 (GM/WM surface) to 1 (GM/CSF surface). The first row shows data from a single participant (P1), thick lines represent the median intensity estimates across cortical depth, shaded lines represent the 95% CI based on 2000 bootstrapping repetitions. The second row shows data from the same participant as in the first row, on the re-test dataset. The third row shows the average data from the 6 datasets, we derived the laminar profiles on each single participant based on the specific definition of area V1 and GM/WM – GM/CSF boundaries, and then averaged the so obtained profiles together. Thick lines represent the mean intensity estimates across cortical depth, shaded lines represent the standard error of the mean across the 6 datasets. T1-w intensity profiles at the single participant and group level show a linear trend with the stronger signal intensity at the GM/WM surface then decreasing towards the GM/CSF surface. Around the middle of the normalized cortical depth we can successfully identify the stria of Gennari (panel A, H and N, dashed and continuous vertical lines represent the 95% CI and the median estimate of peak location). Signal intensity of 3D-EPI mean image for the profiles included in the analysis from the contra-lateral condition (positive %BOLD) shows a clear monotonic increase, as shown in panels B, I and O. Mean %BOLD signal intensity in the contra-lateral condition shows a monotonic increase across all experimental conditions as shown in panel C, J and P, whereas an overall decreasing negative BOLD response can be observed across cortical depth for the ipsi-lateral condition (panels D, K and Q). 3D-EPI mean image signal intensity split into linear trend groups shows a clear monotonic increase, as shown in panels E,L and R. Sorting the profiles according to the strength of the monotonic increase along cortical depth shows different profiles for the weak linear trend group, with a peak in %BOLD signal located around the middle of the normalized cortical depth for the positive BOLD (panels F, M and S, dashed and continuous vertical lines represent the 95% CI and the median estimate of peak location for the weak group). Negative %BOLD signal for the weak linear trend group is relatively flat across cortical depth and shows a monotonic decrease towards the GM/CSF border for the middle and strong trend groups (panels G, N and T, note that the same cortical locations are used in the analysis for the contra- and ipsi-lateral hemifield visual stimulation).

was repeated until the last 3D mesh was reached. The same procedure was adopted to grow the profile towards WM. The two sets of coordinates were merged together to form the coordinate set of a single laminar profile. The GLM results (T-maps and beta-coefficient maps), the 3D-EPI mean image, and the T1-w image were interpolated along the coordinates of each single laminar profile via nearest-neighbor interpolation.

Laminar profiles, selection

All the profiles where the median T statistic along cortical depth for the positive %BOLD condition was higher than 2 ($p < 0.05$, uncorrected) were included for further analysis, to ensure that only locations with a reliable response were analyzed.

To account for small alignment errors and local geometric distortions for each profile, we computed the associated cortical thickness and average T1-w intensity, in order to obtain the distribution of cortical thickness and average T1-w intensity of all the profiles. The 2.5 and 97.5 percentiles of cortical thickness and T1-w intensity percentiles were computed and a profile was excluded if it was smaller than the 2.5 percentile or larger than the 97.5 percentile of cortical thickness or T1-w intensity. On average 1700 laminar profiles were selected for further analysis, for each participant. Each profile included T1-w intensity, 3D-EPI mean image and %BOLD signal change (contra-lateral and ipsi-lateral conditions) per participant.

Laminar profiles, T1-w images

We derived laminar profiles from the T1-w anatomical images. The purpose of this analysis was to identify the highly myelinated stria of Gennari characterizing primary visual cortex (Fracasso et al., 2016b, 2016c). The mean profile for each participant's V1 was obtained by 2000 repetition bootstrapping with resampling. For each iteration, a random set of all the profiles that survived the thresholding were selected, with replacement (Efron and Tibshirani, 1994). From this bootstrapped dataset we obtained the median profile as well the corresponding 95% confidence intervals of the profile. A peak identification algorithm was run on each bootstrapped sample to identify local peaks in the profile. Each profile was interpolated to 100 points between the GM/WM surface and the GM/CSF surface using the function smooth.spline in R (R Development Core Team, http://www.R-project.org). Peaks were identified as positive to negative zero-crossing points of the first derivative of the fit, the corresponding 95% confidence intervals of local peak location were computed.

Analysis of positive and negative %BOLD laminar profiles

The average positive %BOLD profiles show the well known monotonic increase towards the pial surface, in line with previous studies in human and non-human primates using gradient-echo MRI (Chen et al., 2012; De Martino et al., 2013; Fracasso et al., 2016a; Goense and Logothetis, 2006; Koopmans et al., 2011, 2010; Polimeni et al., 2010). To examine the dominance of this monotonic increase across the

profiles we split the dataset into three separate parts, according to the strength of this monotonic increase. For each laminar profile, we then computed the Pearson correlation between the contra-lateral %BOLD profiles and cortical depth. In this way, we obtained a distribution of Pearson correlation coefficients for each participant's V1, representing the strength of the linear trend for each contra-lateral profile. The profiles were then sorted by computing the percentiles of the distribution of the Pearson correlation coefficients. The set of profiles was then divided into three separate subsets: those profiles where the Pearson correlation coefficient was below the 40% quantile (weak linear trend group); those profiles where the Pearson correlation coefficient was above or equal to the 40% quantile and below the 70% quantile (middle linear trend group); and those profiles where the Pearson correlation coefficient was above or equal to the 70% (strong linear trend group).

Next, we averaged all the positive %BOLD profiles for each group. The average profile that emerged for the weak linear trend group was remarkably different from the one obtained by the average of all profiles. In this case, the profile showed a clear peak in activity within gray matter. The median profile of each participant V1 and the positive %BOLD profiles per group were obtained by 2000 repetition bootstrapping with resampling. From this bootstrapped dataset we obtained the median profile as well the corresponding 95% confidence intervals. For each participant V1 and the profiles assigned to the weak linear trend group, the maximum value of the profile was identified and stored on each bootstrapped iteration. The corresponding 95% confidence intervals of peak location were also computed (Fig. 4).

To evaluate the effect of the sorting procedure to the final profile shape, we derived the averaged profile for a set of quantile thresholds iteratively, ranging from 40% of the dataset, to ensure that enough profiles were included in the average, until 100% (the complete dataset). For each iteration, the amplitude of averaged profile was computed and normalized in the [0, 1] range. All the derived profiles are reported as a raster plot, the y-axis reports the corresponding cumulative quantile threshold (from 40% till 100% of the data, see Fig. 5).

Once we identified the laminar profiles based only on activity elicited by contra-lateral visual stimulation (positive %BOLD), we computed the average profile from the profiles for the ipsi-lateral (negative %BOLD) visual stimulation, and sorted the profiles based on the three separate subsets (weak, middle and strong linear trend). Trends in the weak, middle and strong linear trend subsets of positive %BOLD and negative %BOLD were analyzed using linear regression, using a linear and a quadratic parameter model in separate steps. The same analysis was repeated using the slope of the linear model between the contra-lateral %BOLD profiles and cortical depth as a measure to subdivide the profiles in the weak, middle and strong linear trend groups. Sorting profiles using the slope yielded virtually identical results.

B0angle

Human cortex is highly convoluted, as a result a distribution of angles between the cortical surface and the external magnetic field of the MRI scanner (B0) can be observed. Gagnon et al. showed that % BOLD signal varies considerably following the angle between the cortical surface and B0 (Gagnon et al., 2015). This angular dependence likely occurs because pial veins are oriented parallel to the cortical surface. We computed the angle phi (ϕ) between the vector normal to the cortical surface and the B0 vector of the magnet for each of the 3D meshes associated with the 16 level-set surfaces. For each 3D-mesh, the distribution of ϕ angles was divided into 10 separate bins, according to its deciles. For each bin the average %BOLD signal change from the profiles included in the analysis was computed. The predicted relationship between %BOLD and cos $(\phi)^2$ (Gagnon et al., 2015) was tested using least-squares, across cortical depth.

Results

Anatomical profiles identify the stria of Gennari

T1-w intensity profiles show stronger signal intensity at the GM/WM surface then decreasing towards the GM/CSF surface (Figs. 2A, 4A), consistent with previous reports using T1 measurements (Lutti et al., 2013; Sereno et al., 2013). Overall, we can successfully identify the stria of Gennari located around the middle of the normalized cortical depth on the median profiles for each participant's V1, as well as in the average profile of all participants (Fig. 4N, bootstrapped median peak location: 48% of cortical depth).

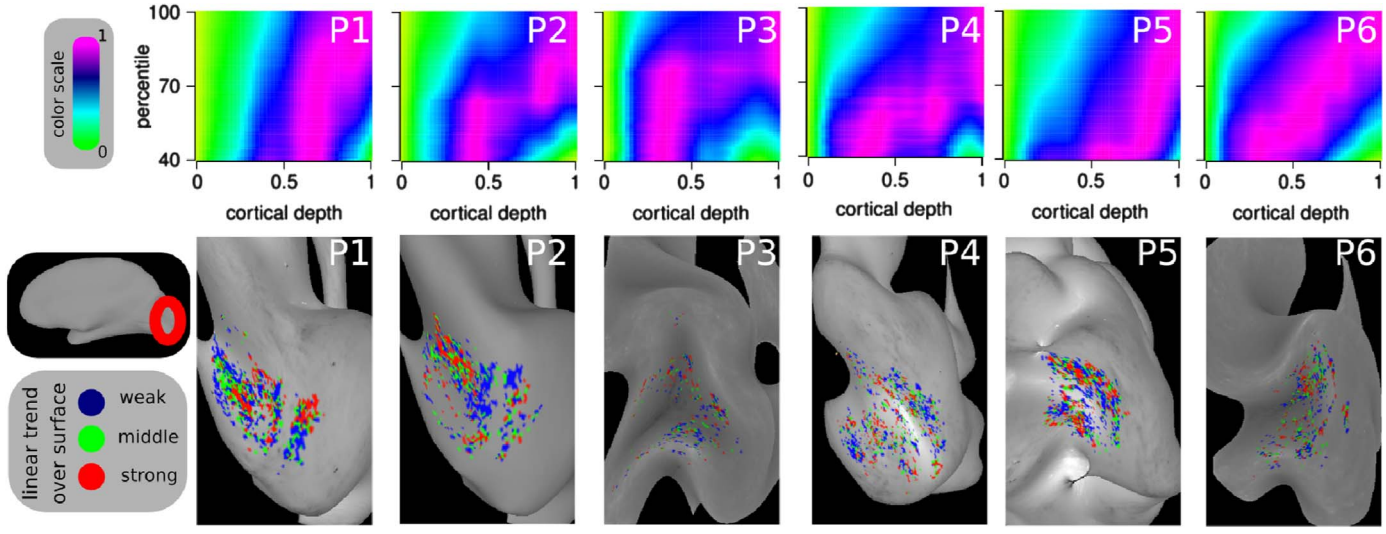

Fig. 5. Rasters of the mean normalized contra-lateral (positive %BOLD) profiles for area V1 as a function of Pearson correlation percentile and distribution of the linear trend groups over the cortical surface P1 and P2 represent the test-retest. Rasters: Y axis, Pearson correlation percentile from 40% and higher; x axis: normalized cortical thickness from GM/WM border (0) to GH/CSF border (1), note that the profiles are all scaled between a minimum of 0 and a maximum of 1 to allow visualization of the rasters independent of the signal amplitude. Different behaviours can be described. In participant 3 (P3) the peak in the middle of cortical thickness remains stable until about 75% of the combined quantile threshold, then the linear trend starts to influence the profile and dominates for the remaining 25% of the data. Alternatively, the linear trend can slowly dominate the profile as is the case for participant P1. Zoomed surfaces on the calcarine fissure (see inset, the perspective on each surface is different to better visualize the calcarine fissure on the right hemisphere across participants), show the distribution of the weak, middle and strong linear trend profile groups across the surface (blue, green and red, respectively, see inset for the legend).

Distinct functional response profiles

The signal intensity of the profiles included in the analysis from the 3D-EPI mean image shows the expected monotonic increase, across all experimental conditions (Figs. 4B, I, O and 3E, L, R), providing a quality check for the realignment of the functional with the structural data. The vast majority of positive %BOLD profiles show a systematic increase towards the GM/CSF surface, likely due to large draining veins at the pial surface (Fig. 4C, J, P). However a proportion of the extracted profiles show a systematic departure from the expected monotonic increase (Fig. 4F, M, S). When the profiles were sorted according to the strength of the monotonic increase along cortical depth, the positive % BOLD profiles in the weak linear trend group showed a remarkably different shape (quadratic predictor across cortical depth, T=7,66, $p < 0.001$), with a peak in %BOLD signal located around the middle of the normalized cortical depth (median bootstrapped peak location: 40% of cortical depth), as could be expected from input-related activity of LGN→V1 afferents in the granular layers of primary visual cortex (Angelucci et al., 2002; Felleman and Van Essen, 1991; Sincich and Horton, 2005), and it is in good agreement with what we observe on T1-w profiles (see '*Anatomical profiles identify the stria of Gennari*').

Rasters of the mean normalized positive %BOLD profiles for area V1, as a function of Pearson correlation percentile, show different behaviors. For example, for participant 3 (P3, Fig. 5) the peak in the middle of cortical thickness remains stable till about 75% of the combined quantile threshold, then the linear trend starts to influence the profile and dominates for the remaining 25% of the data. Alternatively the linear trend can slowly dominate the profile as is the case for participant 1 (P1, Fig. 5).

However, regardless of how the linear trend starts dominating the average profile, average profiles from the weak linear trend group consistently show a peak around the middle of the normalized cortical depth in V1 (Fig. 4 E, L, R). Comparable profiles have been found using neurophysiology (Maier et al., 2011), and fMRI in human (Koopmans et al., 2011; Ress et al., 2007) and non-human primates (Chen et al., 2012). The distribution of weak, middle and strong linear trend profiles across the cortical surface appears to be scattered over the surface renderings, and the different profile groups (weak, middle and strong linear trend groups) tend to form small clusters.

Once we identified the laminar profiles based only on activity elicited by the contra-lateral visual stimulation (positive %BOLD), we computed the average profile from the profiles for the ipsi-lateral visual stimulation (Fig. 4D, K, Q). Absolute %BOLD response in the ipsi-lateral condition is smaller (2–4 times) than the contra-lateral visual stimulation profiles and, on average, shows a monotonic decrease of negative %BOLD signal towards the GM/CSF border (linear predictor across cortical depth: T=12.9, $p < 0.001$), mirroring the contra-lateral %BOLD profiles condition. This pattern was modulated by the linear trend group defined on the contra-lateral %BOLD profiles (see '*Analysis of positive %BOLD and negative %BOLD laminar profiles*'). We observed a decreasing trend for negative %BOLD profile for the profiles in the weak linear trend group (linear predictor across cortical depth: T=5.5, $p < 0.001$), and a gradual strengthening of the monotonic decrease for the profiles in the middle and strong linear trend group (T=7.33 and T=16.07, respectively, Fig. 4G, N, T).

Angular dependence of %BOLD

%BOLD signal changes vary considerably following the angle between the cortical surface and B0 (Gagnon et al., 2015). We computed the angle phi *(ϕ)* between the vector normal to the cortical surface and the magnet B0 vector for each of the 3D mesh associated with 16 level-set surfaces. Results show a strong relation between % BOLD and cos $(\phi)^2$ along each separate 3D-mesh across cortical depth (Fig. 6, average variance explained of the %BOLD dependence with cos $(\phi)^2$, 45% ± 7%). The amplitude of the %BOLD signal was smaller for

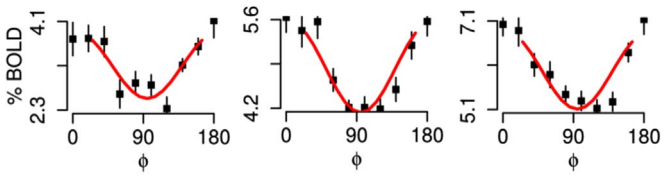

Fig. 6. Angular dependence. %BOLD signal changes vary considerably following the angle between the cortical surface and B0 (ϕ). This relation can be observed along cortical depth. The figure shows the average cortical depth dependence of ϕ across 6 datasets for a 3D-mesh close to WM/GM surface (panel A), around middle cortical depth (panel B) and close to the GM/CSF border (panel C). This relation follows the cos $(\phi)^2$ relation (see red line, representing the least-square fit estimate for each 3D-mesh).

angles close to 90° across cortical depth, and the signal increased towards the pial surface irrespective of the angle to B0. The average ϕ along cortical depth did not correlate with the strength of the linear trend across cortical depth (average Pearson correlation across 6 datasets: 0.03 ± 0.08), indicating that the pattern across cortical depth is not dominated by the B0 angle effect, although the amplitude is (Fig. 6).

Discussion

Results summary

We acquired functional 3D-EPI data at 0.55 mm isotropic spatial resolution to derive positive and negative %BOLD activity profiles across cortical depth. We derived T1-w intensity profiles across cortical depth corresponding to the BOLD laminar profiles (see Methods and Fig. 4A, H). The average T1-w profiles (Fig. 4H) show that we can successfully identify the highly myelinated stria of Gennari located around the middle of normalized cortical depth of the median profiles of each single participant's primary visual cortex, as well as in the average profile of all participants (Fig. 4N). These results validate the equi-volume model adopted here in primary visual cortex, in humans, in-vivo, further suggesting that it might provide the basis for a standard analysis pipeline for laminar imaging (Waehnert et al., 2016, 2014).

While participants viewed the stimuli with the grating spokes randomly changing direction at a relatively fast pace (~1.7 Hz), they were asked to press a button whenever they detected a change. Their average percent correct is 70%, which shows that they can perform the task, but it is challenging nonetheless. We employed a demanding task because it has been shown, using a similar unilateral stimulation paradigm, that negative %BOLD signal change is strongly modulated by the presence of a task in the unstimulated hemisphere (Gouws et al., 2014). Here we take advantage of this observation in order to maximize the negative %BOLD signal in our ipsi-lateral condition.

Only a portion of primary visual cortex was stimulated in our visual paradigm (see the spatial extent of BOLD activity in Fig. 1 compared to the V1/V2 border location), resulting in an under-representation of the vertical meridian. We opted for this kind of visual stimulation in order to minimize the influence of eye movements in the contra-lateral/ipsi-lateral separation (see Fig. 1A and B). Otherwise, small eye movements towards the left or right side of the visual stimulation would have confounded the distinction between contra-lateral/ipsi-lateral conditions.

We report different %BOLD laminar profiles associated with contra-lateral and ipsi-lateral signal sources in primary visual cortex, V1 (Fig. 4F, M). Retino-cortical afferents reach V1 at granular layer 4C, then, as early as the second synapse, the signal rapidly spreads across laminae (Self et al., 2013; Sincich and Horton, 2005). Despite the relatively low temporal resolution that characterizes fMRI, we measure laminar profiles identifying the location of input-related activity at the level of the stria of Gennari. Moreover, we took advantage of our visual paradigm to go a step further, analyzing the shape of the laminar profile associated with suppressive signals presumably relayed via

inter-hemispheric connections. The suppressive inter-hemispheric signal was characterized by a decrease in %BOLD signal in response to the ipsilateral visual stimulation and smaller signal amplitude (2–4 times, Fig. 4D, K and Fig. 4G, N). Overall we show that the combination of structural and functional data with high contrast at a comparable resolution is an extremely powerful approach to cross-validate functional data with anatomical features.

Contra-lateral (positive %BOLD) profiles

The average positive %BOLD profiles exhibited a monotonic increase toward the pial surface in line with previous reports (Chen et al., 2012; De Martino et al., 2013; Fracasso et al., 2016a; Koopmans et al., 2012, 2011; Siero et al., 2011; Zimmermann et al., 2011), as expected from the known sensitivity of gradient-echo BOLD to larger pial veins that drain blood from several intra-cortical sites (Kim and Ogawa, 2012; Turner, 2002).

We observe high signal at the level of the WM (between 2% and 4% BOLD signal change). This result is compatible with what has been reported previously in the literature using gradient echo sequences (De Martino et al., 2013, Fracasso et al., 2016a). Several elements might explain this high signal at the level of the WM: registration and segmentation errors, the blurring introduced by participant motion and T2* blurring could contribute to blur the signal specificity.

However, for each individual participant, the shape of the %BOLD profiles that contributed to the single-participant average profile varied considerably. For each participant, a group of profiles exhibited a peak around the middle of the cortical thickness (Fig. 5, raster plots) which could reflect signals originating from venules and/or micro-vasculature supplying the input layer in V1. The estimated location of the peak in the weak linear trend group of profiles was similar to the peak location in the T1-w anatomical profiles, corresponding to the stria of Gennari (Barbier et al., 2002; Duyn et al., 2007; Fracasso et al., 2016b, 2016c; Gennari, 1782) (see Figs. 2, 4A, H and F, M). A different group of profiles was dominated by the monotonic increase in %BOLD signal change toward the pial surface (Fig. 5, raster plots), likely reflecting larger signals from the pial vasculature. This monotonic increase appeared either gradually or distinctly between subjects. The source of this difference between subjects is unclear but could be due to differences in the distribution of profiles that passed the selection criteria (see '*Laminar profiles, selection*'), for example due to differences in the T-values between subjects. Differences in vascular anatomy or small co-registration errors that become significant at this high acquisition resolution might also play a role. One possible way to overcome small co-registration errors would be to correct the EPI data using a top-up procedure (blip-up/blip down), in order to compensate for non-linear distortions that a simple affine transformation cannot account for (Muckli et al., 2016). Another viable strategy might be the use of a T1-w 3D-EPI acquisition, in order to obtain an EPI volume (and the associated geometric distortions) but with a T1 contrast that could aid the coregistration with the actual T1-w anatomy for each single participant (Kashyap et al., 2016; van der Zwaag et al., 2016).

A possible explanation for the differences in the shape of the profiles within subjects, that is, the presence or absence of a peak around the middle of the cortical thickness, could be the extent to which a pial vein was included in a given profile, translating to different signal contributions from the pial surface. Another possibility could be small realignment errors or local distortions in the 3D-EPI space compared to the T1-w space. The very high spatial resolution employed here (0.55 mm isotropic) could have allowed the sensitivity to spatial variations in pial vein organization. The distribution of weak, middle and strong linear trend profiles across the cortical surface appears to be randomly scattered, in small clusters, (Fig. 4), which could also be related different sources of blurring in the data, for example registration and segmentation errors, as well as the blurring introduced by participant motion and T2* blurring.

Ipsi-lateral (negative BOLD) profiles

The laminar profile in the ipsi-lateral condition, associated with the suppressive inter-hemispheric signal source, showed an average monotonic decrease of the %BOLD signal towards the pial surface.

Multiple mechanisms have been described as a source of negative BOLD. Decreases in BOLD signal in response to visual stimuli are associated with both decreased neural firing rate as well as a decrease in local field potentials below spontaneous activity, especially when the source of the negative BOLD signal is located far from the source of the positive BOLD signal (Shmuel et al., 2006).

Previously reported studies show larger negative BOLD response in deeper than superficial portions of the gray matter (Boorman, 2010; Goense 2012; Huber, 2014). This is different compared with what we report, as we show a larger response for superficial than deeper portions of the cortex. One major methodological difference between our study and the reported findings is the type of visual paradigm used. In our visual stimulation, negative BOLD is elicited in portions of the cortex located in the opposite hemisphere (Gouws et al., 2014). In previous studies, negative BOLD was elicited in the same hemisphere and in neighboring cortical locations as the positive BOLD. These negative BOLD signals elicited by inter-hemispheric communication versus between neighboring cortical locations within one hemisphere may be very different.

A reduction in neural activity can lead to a negative BOLD response, associated with a negative cerebral blood flow (CBF) response and a negative cerebral blood volume (CBV) response (Boorman et al., 2010). Goense et al. (2012), however, reported negative BOLD response in the surrounding of a stimulated area in the visual cortex, together with a negative CBF response and a positive CBV response. Shmuel et al. (2006, 2002) report a negative BOLD response together with negative CBF response, negative oxygen consumption response and a decrease in neuronal activity. However, the results in the literature are not conclusive concerning the exact mechanism underlying the source of negative BOLD signal. Data acquired across different species on a similar ROI (monkey and human primary visual cortex) and using the same VASO sequence yielded different results on the CBV change associated with negative BOLD response between the different species. Huber et al. (2014) measured VASO signal changes from monkey primary visual cortex, in an ROI where negative BOLD signal was observed, reporting negative VASO changes associated with CBV increase in the area. Whereas in humans positive VASO changes were observed, associated with a decrease in CBV. A negative BOLD response has also been associated to a blood flow redistribution with a decrease in CBV, also referred to as the “blood- steal” effect (Harel et al., 2002). The latter mechanism can account for negative BOLD signal located in close proximity to the positive BOLD signal, thus it is an unlikely explanation for our observation, given that the source of negative BOLD is located in the opposite hemisphere with respect to the source of the positive BOLD. We observe negative BOLD without the confounding effect of 'blood-stealing', in line with the neurophysiological origin of negative BOLD (Shmuel et al., 2006). It has been shown that the hemodynamic response function differs between positive and negative BOLD responses (Huber et al., 2014, 2015), however, given the block design employed here and the relatively slow TR adopted to achieve the 0.55 mm nominal acquisition resolution, it is unlikely that differences in hemodynamic response shape between positive and negative BOLD responses would bias our results.

We observe a steady monotonic decrease of BOLD signal across cortical depth, mirroring what is usually observed with positive BOLD. This result is similar to what has been observed with non-human primates (Goense et al., 2012). Dividing the profiles into weak/middle/strong linear trend groups (based on the contra-lateral BOLD signal) revealed a moderate monotonic decrease of negative BOLD profile across cortical depth for the weak linear trend group (Fig. 4D, K, Q and G, N, T), suggesting that the shape of the profile may potentially

include features that reflect laminar functional organization, isolating feed-forward activity in human primary visual cortex. The source of this negative BOLD profile may be mediated by suppressive interaction, following inter-hemispheric communication through callosal connections (Van Essen et al., 1982) or cortico-cortical suppressive interaction mediated by the corpus callosum through contralateral V4 (Desimone et al., 1993). However it could be due to known extra-striate afferents in V1, mediating extra-classical receptive fields effects outside the range of horizontal connections inside V1 (Angelucci et al., 2002; Zuiderbaan et al., 2012). However, the amplitude of negative BOLD was 2–4 times smaller than the amplitude of the positive BOLD, therefore more sensitivity than allowed in the present study is likely needed to elucidate the exact features of negative BOLD profiles across cortical depth, in the absence of any 'blood-stealing' contribution.

Angle with respect to B0

Human cortex is highly convoluted, as a result a distribution of angles between the cortical surface and the external magnetic field of the MRI scanner (B0) can be observed. Gagnon and colleagues showed that %BOLD signal varies as a function of the angle between the cortical surface and B0 (Gagnon et al., 2015). This relation is probably due to the presence of pial veins that are oriented parallel to the cortical surface. Here, we observe the angular dependence of %BOLD amplitude varying with respect to angle across all depths (Fig. 6). A proportion of veins are oriented perpendicular to the cortical surface, however, the diameter of pial veins is larger compared with the diameter of ascending veins (Blinder et al., 2013), and pial veins are reflected more strongly in the %BOLD signal (Fig. 4), which could explain our results across cortical depth. High resolution functional images were collected using T2*-w gradient-echo fMRI which is known to be sensitive to vascular components biased towards signal from large draining pial veins located at the GM surface. Modeling results suggest that the angular dependence shown here should not be observed when using T2-w sequences. Nevertheless, our results show a linear increase of the BOLD amplitude across cortical depth irrespective of the angle with respect to B0, and lack of correlation between average angle at the single profile level and single profile linear trend.

Methodological considerations

Recent studies show that CBV based fMRI, for example using a VASO sequence, can have a higher specificity for the microvasculature within gray matter, than to the pial surface (Huber et al., 2014, p. 201; Jin and Kim, 2008)). Attempts have been made to increase the spatial specificity of the BOLD signal by moving towards spin-echo (Goense et al., 2007) and, more recently, 3D GRASE sequences (De Martino et al., 2013). However, while the aforementioned T2-weighted sequences can show increased spatial specificity towards the capillary bed, they also come at a reduced BOLD contrast and typically cover a fairly small region of cortex (De Martino et al., 2013). For gradient-echo EPI at high spatial resolution, areas of large draining veins located around the pial surface can be excluded or avoided to improve the spatial specificity to cortical gray matter (Koopmans et al., 2010; Polimeni et al., 2010). In the present investigation, we show that using gradient-echo EPI at increased submillimeter resolutions (0.55 mm isotropic) it is possible to isolate %BOLD laminar profiles showing higher sensitivity to signals originating around the middle of the cortical depth, likely reflecting the microvasculature compartment along cortical depth. In order to achieve the high functional spatial resolution reported here we largely decreased our temporal resolution, employing a TR of 6.5. Recent advances in coil developments and accelerated acquisitions such as CAIPIRINHA (Setsompop et al., 2016) will be essential to improve the temporal resolution of sub-millimeter fMRI.

The acquired fMRI images can be degraded by participant motion inside the scanner. Using experienced participants might alleviate the problem, but this is not a winning strategy in the long term, excluding for example the possibility of running large cohort studies and limiting research to smaller pools of selected participants, as in the present study. The use of prospective motion correction (Gallichan et al., 2016; Gallichan and Marques, 2016; Qin et al., 2009) to minimize motion artifacts, should help reduce this problem, which constitutes a clear burden, especially for the clinical usage of sub-millimeter resolution fMRI and MRI.

Even when subject motion is minimized by using experienced participants, the accuracy of co-registration needs to be excellent between functional scans and with anatomical scans in different modalities, to preserve as much as possible the level of anatomical detail and the correspondence between anatomical and functional data. High resolution structural data is normally manually segmented (or segmentation is manually corrected after a first automatic pass) and can be performed on a high-resolution T1-image or directly on the 3D-EPI space, with similar results (Fracasso et al., 2016a).

Measuring intensity across cortical depth in humans necessitates isotropic resolutions given that the human brain highly gyrified than other animal brains. However this convoluted structure complicates the analysis of the data, given that cortical thickness is not uniform across the cortex and biased, being thicker on the sulci compared to in the gyri. Specialized data analysis pipelines are needed to deal with this kind of data, accounting for these geometrical biases. The equi-volume model adopted here represents a validated approach (Waehnert et al., 2014) that builds a coordinate system along cortical depth taking local curvature into account. This approach might provide the basis for a standard analysis pipeline for laminar imaging, with functional and structural data (Waehnert et al., 2016, 2014).

Conclusion

In sum, we show that using careful data analysis strategies and considering the advantages and the limitations of gradient echo EPI sequences, laminar imaging might help to bridge the gap between neurophysiology and functional imaging, informing about the specificity of the signal along the laminar profile. The shape of individual positive %BOLD profiles that contributed to the average profile per individual varied, with a group of profiles exhibiting a peak around the middle of the cortical thickness. This could reflect signals originating from venules and/or micro-vasculature supplying the input layer in V1. Negative %BOLD profiles show a monotonic decrease of BOLD signal across cortical depth, mirroring what is usually observed with positive %BOLD. Further we demonstrate that the equi-volume model might provide the basis for a standard analysis pipeline for laminar imaging in humans, in vivo, with functional and anatomical data (Waehnert et al., 2016, 2014).

Acknowledgments

This work has supported by Ammodo KNAW Award 2015 (S.D.) and a Netherlands Organization for Scientific Research (NWO) Vidi Grant 13339 (N.P.). The Spinoza Centre is a joint initiative of the University of Amsterdam, Academic Medical Center, VU University, VU University Medical Center, Netherlands Institute for Neuroscience and the Royal Netherlands Academy of Science.

References

Amano, K., Wandell, B.A., Dumoulin, S.O., 2009. Visual field maps, population receptive field sizes, and visual field coverage in the human MT+ complex. J. Neurophysiol. 102, 2704–2718. http://dx.doi.org/10.1152/jn.00102.2009.

Angelucci, A., Levitt, J.B., Walton, E.J.S., Hupe, J.-M., Bullier, J., Lund, J.S., 2002. Circuits for local and global signal integration in primary visual cortex. J. Neurosci. Off. J. Soc. Neurosci. 22, 8633–8646.

Barbier, E.L., Marrett, S., Danek, A., Vortmeyer, A., van Gelderen, P., Duyn, J.,

Bandettini, P., Grafman, J., Koretskyk, A.P., 2002. Imaging cortical anatomy by high-resolution MR at 3.0 T: detection of the stripe of Gennari in visual area 17. Magn. Reson. Med. 48, 735–738. http://dx.doi.org/10.1002/mrm.10255.

Bazin, P.-L., Cuzzocreo, J.L., Yassa, M.A., Gandler, W., McAuliffe, M.J., Bassett, S.S., Pham, D.L., 2007. Volumetric neuroimage analysis extensions for the MIPAV software package. J. Neurosci. Methods 165, 111–121. http://dx.doi.org/10.1016/j.jneumeth.2007.05.024.

Blinder, P., Tsai, P.S., Kaufhold, J.P., Knutsen, P.M., Suhl, H., Kleinfeld, D., 2013. The cortical angiome: an interconnected vascular network with noncolumnar patterns of blood flow. Nat. Neurosci. 16, 889–897. http://dx.doi.org/10.1038/nn.3426.

Bock, N.A., Kocharyan, A., Liu, J.V., Silva, A.C., 2009. Visualizing the entire cortical myrelination pattern in marmosets with magnetic resonance imaging. J. Neurosci. Methods 185, 15–22. http://dx.doi.org/10.1016/j.jneumeth.2009.08.022.

Boorman, L., Kennerley, A.J., Johnston, D., Jones, M., Zheng, Y., Redgrave, P., Berwick, J., 2010. Negative blood oxygen level dependence in the rat: a model for investigating the role of suppression in neurovascular coupling. J. Neurosci. Off. J. Soc. Neurosci. 30, 4285–4294. http://dx.doi.org/10.1523/JNEUROSCI.6063-09.2010.

Brainard, D.H., 1997. Psychophys. Toolbox Spat. Vis. 10, 433–436.

Callaway, E.M., 1998. Prenatal development of layer-specific local circuits in primary visual cortex of the macaque monkey. J. Neurosci. Off. J. Soc. Neurosci. 18, 1505–1527.

Chen, G., Wang, F., Gore, J.C., Roe, A.W., 2012. Identification of cortical lamination in awake monkeys by high resolution magnetic resonance imaging. Neuroimage 59, 3441–3449. http://dx.doi.org/10.1016/j.neuroimage.2011.10.079.

Cox, R.W., 1996. AFNI: software for analysis and visualization of functional magnetic resonance neuroimages. Comput. Biomed. Res. Int. J. 29, 162–173.

De Martino, F., Zimmermann, J., Muckli, L., Ugurbil, K., Yacoub, E., Goebel, R., 2013. Cortical depth dependent functional responses in humans at 7 T: improved specificity with 3D GRASE. PLoS One 8, e60514. http://dx.doi.org/10.1371/journal.pone.0060514.

Desimone, R., Moran, J., Schein, S.J., Mishkin, M., 1993. A role for the corpus callosum in visual area V4 of the macaque. Vis. Neurosci. 10, 159–171.

Dumoulin, S.O., Wandell, B.A., 2008. Population receptive field estimates in human visual cortex. NeuroImage 39, 647–660. http://dx.doi.org/10.1016/j.neuroimage.2007.09.034.

Duyn, J.H., van Gelderen, P., Li, T.-Q., de Zwart, J.A., Koretsky, A.P., Fukunaga, M., 2007. High-field MRI of brain cortical substructure based on signal phase. Proc. Natl. Acad. Sci. USA 104, 11796–11801. http://dx.doi.org/10.1073/pnas.0610821104.

Efron, B., Tibshirani, R.J., 1994. An Introduction to the Bootstrap. CRC Press, Boca Raton, FL.

Felleman, D.J., Van Essen, D.C., 1991. Distributed hierarchical processing in the primate cerebral cortex. Cereb. Cortex N. Y. N 1991 1, 1–47.

Fracasso, A., Petridou, N., Dumoulin, S.O., 2016a. Systematic variation of population receptive field properties across cortical depth in human visual cortex. NeuroImage 139, 427–438. http://dx.doi.org/10.1016/j.neuroimage.2016.06.048.

Fracasso, A., van Veluw, S.J., Visser, F., Luijten, P.R., Spliet, W., Zwanenburg, J.J.M., Dumoulin, S.O., Petridou, N., 2016b. Lines of Baillarger in vivo and ex vivo: myelin contrast across lamina at 7 T MRI and histology. NeuroImage 133, 163–175. http://dx.doi.org/10.1016/j.neuroimage.2016.02.072.

Fracasso, A., van Veluw, S.J., Visser, F., Luijten, P.R., Spliet, W., Zwanenburg, J.J.M., Dumoulin, S.O., Petridou, N., 2016c. Myelin contrast across lamina at 7 T, ex-vivo and in-vivo dataset. Data Brief 8, 990–1003. http://dx.doi.org/10.1016/j.dib.2016.06.058.

Gagnon, L., Sakadžić, S., Lesage, F., Musacchia, J.J., Lefebvre, J., Fang, Q., Yücel, M.A., Evans, K.C., Mandeville, E.T., Cohen-Adad, J., Polimeni, J.R., Yaseen, M.A., Lo, E.H., Greve, D.N., Buxton, R.B., Dale, A.M., Devor, A., Boas, D.A., 2015. Quantifying the microvascular origin of BOLD-fMRI from first principles with two-photon microscopy and an oxygen-sensitive nanoprobe. J. Neurosci. Off. J. Soc. Neurosci. 35, 3663–3675. http://dx.doi.org/10.1523/JNEUROSCI.3555-14.2015.

Gallichan, D., Marques, J.P., 2016. Optimizing the acceleration and resolution of three-dimensional fat image navigators for high-resolution motion correction at 7 T. Magn. Reson. Med.. http://dx.doi.org/10.1002/mrm.26127.

Gallichan, D., Marques, J.P., Gruetter, R., 2016. Retrospective correction of involuntary microscopic head movement using highly accelerated fat image navigators (3D FatNavs) at 7 T. Magn. Reson. Med. 75, 1030–1039. http://dx.doi.org/10.1002/mrm.25670.

Gennari F., 1782. De Peculiari Structura Cerebri. Nonnullisque ejus morbis. Ex Regio Typographeo, Parma.

Goense, J., Merkle, H., Logothetis, N.K., 2012. High-resolution fMRI reveals laminar differences in neurovascular coupling between positive and negative BOLD responses. Neuron 76, 629–639. http://dx.doi.org/10.1016/j.neuron.2012.09.019.

Goense, J.B.M., Logothetis, N.K., 2006. Laminar specificity in monkey V1 using high-resolution SE-fMRI. Magn. Reson. Imaging 24, 381–392. http://dx.doi.org/10.1016/j.mri.2005.12.032.

Goense, J.B.M., Zappe, A.-C., Logothetis, N.K., 2007. High-resolution fMRI of macaque V1. Magn. Reson. Imaging 25, 740–747. http://dx.doi.org/10.1016/j.mri.2007.02.013.

Gouws, A.D., Alvarez, I., Watson, D.M., Uesaki, M., Rodgers, J., Morland, A.B., 2014. On the Role of Suppression in Spatial Attention: evidence from Negative BOLD in Human Subcortical and Cortical Structures. J. Neurosci. 34 (42), 14164–114164.

Guidi, M., Huber, L., Lampe, L., Gauthier, C.J., Möller, H.E., 2016. Lamina-dependent calibrated BOLD response in human primary motor cortex. NeuroImage 141, 250–261. http://dx.doi.org/10.1016/j.neuroimage.2016.06.030.

Haacke, E.M., Brown, R.W., Cheng, Y.N., Thompson, M.R., Venkatesan, R., 1999. Magnetic Resonance Imaging: Physical Principles and Sequence Design. John Wiley & Sons, New York, NY.

Harel, N., Lee, S.P., Nagaoka, T., Kim, D.S., Kim, S.G., 2002. Origin of negative blood oxygenation level—dependent fMRI signals. J. Cerebr. Blood F. Met. 22 (8), 908–917.

Harvey, B.M., Dumoulin, S.O., 2011. The relationship between cortical magnification factor and population receptive field size in human visual cortex: constancies in cortical architecture. J. Neurosci. Off. J. Soc. Neurosci. 31, 13604–13612. http://dx.doi.org/10.1523/JNEUROSCI.2572-11.2011.

Huber, L., Goense, J., Kennerley, A.J., Ivanov, D., Krieger, S.N., Lepsien, J., Trampel, R., Turner, R., Möller, H.E., 2014. Investigation of the neurovascular coupling in positive and negative BOLD responses in human brain at 7 T. NeuroImage 97, 349–362. http://dx.doi.org/10.1016/j.neuroimage.2014.04.022.

Huber, L., Goense, J., Kennerley, A.J., Trampel, R., Guidi, M., Reimer, E., Ivanov, D., Neef, N., Gauthier, C.J., Turner, R., Möller, H.E., 2015. Cortical lamina-dependent blood volume changes in human brain at 7 T. NeuroImage 107, 23–33. http://dx.doi.org/10.1016/j.neuroimage.2014.11.046.

Jin, T., Kim, S.G., 2008. Cortical layer-dependent dynamic blood oxygenation, cerebral blood flow and cerebral blood volume responses during visual stimulation. Neuroimage 43, 1–9. http://dx.doi.org/10.1016/j.neuroimage.2008.06.029.

Kashyap, S., Ivanov, I., Havlícek, M., Poser, M.A., Uludag, K., 2016. High-resolution T1-Mapping Using Inversion-recovery EPI and Application to Cortical Depth-dependent fMRI at 7 T. International Society for Magnetic Resonance in Medicine (ISMRM), Singapore.

Kim, S.-G., Ogawa, S., 2012. Biophysical and physiological origins of blood oxygenation level-dependent fMRI signals. J. Cereb. Blood Flow Metab. Off. J. Int. Soc. Cereb. Blood Flow Metab. 32, 1188–1206. http://dx.doi.org/10.1038/jcbfm.2012.23.

Koopmans, P.J., Barth, M., Norris, D.G., 2010. Layer-specific BOLD activation in human V1. Hum. Brain Mapp. 31, 1297–1304. http://dx.doi.org/10.1002/hbm.20936.

Koopmans, P.J., Barth, M., Orzada, S., Norris, D.G., 2011. Multi-echo fMRI of the cortical laminae in humans at 7 T. NeuroImage 56, 1276–1285. http://dx.doi.org/10.1016/j.neuroimage.2011.02.042.

Koopmans, P.J., Boyacioğlu, R., Barth, M., Norris, D.G., 2012. Whole brain, high resolution spin-echo resting state fMRI using PINS multiplexing at 7 T. NeuroImage 62, 1939–1946. http://dx.doi.org/10.1016/j.neuroimage.2012.05.080.

Logothetis, N.K., Pauls, J., Augath, M., Trinath, T., Oeltermann, A., 2001. Neurophysiological investigation of the basis of the fMRI signal. Nature 412, 150–157. http://dx.doi.org/10.1038/35084005.

Lund, J.S., 1988. Anatomical organization of macaque monkey striate visual cortex. Annu. Rev. Neurosci. 11, 253–288. http://dx.doi.org/10.1146/annurev.ne.11.030188.001345.

Lutti, A., Dick, F., Sereno, M.I., Weiskopf, N., 2013. Using high-resolution quantitative mapping of R1 as an index of cortical myelination. Neuroimage.

Maier, A., Aura, C.J., Leopold, D.A., 2011. Infragranular sources of sustained local field potential responses in macaque primary visual cortex. J. Neurosci. Off. J. Soc. Neurosci. 31, 1971–1980. http://dx.doi.org/10.1523/JNEUROSCI.5300-09.2011.

Muckli, L., De Martino, F., Vizioli, L., Petro, L.S., Smith, F.W., Ugurbil, K., Goebel, R., Yacoub, E., 2015. Contextual feedback to superficial layers of V1. Curr. Biol. 25 (20), 2690-–22695.

Olman, C.A., Harel, N., Feinberg, D.A., He, S., Zhang, P., Ugurbil, K., Yacoub, E., 2012. Layer-specific fMRI reflects different neuronal computations at different depths in human V1. PLoS One 7, e32536. http://dx.doi.org/10.1371/journal.pone.0032536.

Pelli, D.G., 1997. The VideoToolbox software for visual psychophysics: transforming numbers into movies. Spat. Vis. 10, 437–442.

Petridou, N., Italiaander, M., van de Bank, B.L., Siero, J.C.W., Luijten, P.R., Klomp, D.W.J., 2013. Pushing the limits of high-resolution functional MRI using a simple high-density multi-element coil design. NMR Biomed. 26, 65–73. http://dx.doi.org/10.1002/nbm.2820.

Polimeni, J.R., Fischl, B., Greve, D.N., Wald, L.L., 2010. Laminar analysis of 7 T BOLD using an imposed spatial activation pattern in human V1. NeuroImage 52, 1334–1346. http://dx.doi.org/10.1016/j.neuroimage.2010.05.005.

Qin, L., van Gelderen, P., Derbyshire, J.A., Jin, F., Lee, J., de Zwart, J.A., Tao, Y., Duyn, J.H., 2009. Prospective head-movement correction for high-resolution MRI using an in-bore optical tracking system. Magn. Reson. Med. Off. J. Soc. Magn. Reson. Med. Soc. Magn. Reson. Med 62, 924–934. http://dx.doi.org/10.1002/mrm.22076.

Ress, D., Glover, G.H., Liu, J., Wandell, B., 2007. Laminar profiles of functional activity in the human brain. NeuroImage 34, 74–84. http://dx.doi.org/10.1016/j.neuroimage.2006.08.020.

Saad, Z.S., Glen, D.R., Chen, G., Beauchamp, M.S., Desai, R., Cox, R.W., 2009. A new method for improving functional-to-structural MRI alignment using local Pearson correlation. NeuroImage 44, 839–848. http://dx.doi.org/10.1016/j.neuroimage.2008.09.037.

Self, M.W., van Kerkoerle, T., Supèr, H., Roelfsema, P.R., 2013. Distinct roles of the cortical layers of area V1 in figure-ground segregation. Curr. Biol. CB 23, 2121–2129 . http://dx.doi.org/10.1016/j.cub.2013.09.013.

Sereno, M.I., Lutti, A., Weiskopf, N., Dick, F., 2013. Mapping the human cortical surface by combining quantitative T(1) with retinotopy. Cereb. Cortex N. Y. N 23, 2261–2268. http://dx.doi.org/10.1093/cercor/bhs213.

Setsompop, K., Feinberg, D.A., Polimeni, J.R., 2016. Rapid brain MRI acquisition techniques at ultra-high fields. NMR Biomed. 29, 1198–1221. http://dx.doi.org/10.1002/nbm.3478.

Shmuel, A., Augath, M., Oeltermann, A., Logothetis, N.K., 2006. Negative functional MRI response correlates with decreases in neuronal activity in monkey visual area V1. Nat. Neurosci. 9, 569–577. http://dx.doi.org/10.1038/nn1675.

Shmuel, A., Yacoub, E., Pfeuffer, J., Van de Moortele, P.F., Adriany, G., Hu, X., Ugurbil, K., 2002. Sustained negative BOLD, blood flow and oxygen consumption response

and its coupling to the positive response in the human brain. Neuron 36, 1195–1210.
Siero, J.C.W., Petridou, N., Hoogduin, H., Luijten, P.R., Ramsey, N.F., 2011. Cortical depth-dependent temporal dynamics of the BOLD response in the human brain. J. Cereb. Blood Flow Metab. Off. J. Int. Soc. Cereb. Blood Flow Metab. 31, 1999–2008. http://dx.doi.org/10.1038/jcbfm.2011.57.
Siero, J.C.W., Ramsey, N.F., Hoogduin, H., Klomp, D.W.J., Luijten, P.R., Petridou, N., 2013. BOLD specificity and dynamics evaluated in humans at 7 T: comparing gradient-echo and spin-echo hemodynamic responses. PLoS One 8, e54560. http://dx.doi.org/10.1371/journal.pone.0054560.
Sincich, L.C., Horton, J.C., 2005. The circuitry of V1 and V2: integration of color, form, and motion. Annu. Rev. Neurosci. 28, 303–326. http://dx.doi.org/10.1146/annurev.neuro.28.061604.135731.
Tootell, R.B., Hadjikhani, N.K., Vanduffel, W., Liu, A.K., Mendola, J.D., Sereno, M.I., Dale, A.M., 1998. Functional analysis of primary visual cortex (V1) in humans. Proc. Natl. Acad. Sci. USA 95, 811–817.
Turner, R., 2002. How much cortex can a vein drain? Downstream dilution of activation-related cerebral blood oxygenation changes. Neuroimage 16 (4), 1062-–11067.
Van Essen, D.C., Newsome, W.T., Bixby, J.L., 1982. The pattern of interhemispheric connections and its relationship to extrastriate visual areas in the macaque monkey. J. Neurosci. Off. J. Soc. Neurosci. 2, 265–283.
Waehnert, M.D., Dinse, J., Schäfer, A., Geyer, S., Bazin, P.-L., Turner, R., Tardif, C.L., 2016. A subject-specific framework for in vivo myeloarchitectonic analysis using high resolution quantitative MRI. NeuroImage 125, 94–107. http://dx.doi.org/10.1016/j.neuroimage.2015.10.001.
Waehnert, M.D., Dinse, J., Weiss, M., Streicher, M.N., Waehnert, P., Geyer, S., Turner, R., Bazin, P.-L., 2014. Anatomically motivated modeling of cortical laminae. NeuroImage 93 (Pt2), 210–220. http://dx.doi.org/10.1016/j.neuroimage.2013.03.078.
Winawer, J., Horiguchi, H., Sayres, R.A., Amano, K., Wandell, B.A., 2010. Mapping hV4 and ventral occipital cortex: the venous eclipse. J. Vis. 10, 1.
Zilles, K., Palomero-Gallagher, N., Schleicher, A., 2004. Transmitter receptors and functional anatomy of the cerebral cortex. J. Anat. 205, 417–432. http://dx.doi.org/10.1111/j.0021-8782.2004.00357.x.
Zimmermann, J., Goebel, R., De Martino, F., van de Moortele, P.-F., Feinberg, D., Adriany, G., Chaimow, D., Shmuel, A., Uğurbil, K., Yacoub, E., 2011. Mapping the organization of axis of motion selective features in human area MT using high-field fMRI. PLoS One 6, e28716. http://dx.doi.org/10.1371/journal.pone.0028716.
Zuiderbaan, W., Harvey, B.M., Dumoulin, S.O., 2012. Modeling center-surround configurations in population receptive fields using fMRI. J. Vis. 12, 10. http://dx.doi.org/10.1167/12.3.10.
van der Zwaag, W., Buur, P., Versluis, M., Marques, J.P., 2016. Distortion-matched T1-maps and Bias-corrected T1w-images as Anatomical Reference for Submillimeter-resolution fMRI. International Society for Magnetic Resonance in Medicine (ISMRM), Singapore.